Journal of Power Sources 492 (2021) 229660

Contents lists available at ScienceDirect

Journal of Power Sources

journal homepage: www.elsevier.com/locate/jpowsour

Synchrotron X-Ray radiography of vanadium redox flow batteries – Time and spatial resolved electrolyte flow in porous carbon electrodes

Kerstin Köble [a], László Eifert [a], Nico Bevilacqua [a], Kieran F. Fahy [b], Aimy Bazylak [b], Roswitha Zeis [a,*]

[a] Karlsruhe Institute of Technology, Helmholtz Institute Ulm, Helmholtzstraße 11, D-89081, Ulm, Germany
[b] Thermofluids for Energy and Advanced Materials (TEAM) Laboratory, Department of Mechanical & Industrial Engineering, University of Toronto, Institute for Sustainable Energy, Faculty of Applied Science & Engineering, University of Toronto, 5 King's College Road, Toronto, Ontario, M5S 3G8, Canada

HIGHLIGHTS

- Visualization of the electrolyte flow in a battery electrode using X-ray radiography.
- Impact of different flow field configurations and compressions on the electrolyte invasion.
- Time and spatial resolved electrolyte saturation is quantified.
- Influence of manufacturing and boundary features on the electrolyte propagation.

GRAPHICAL ABSTRACT

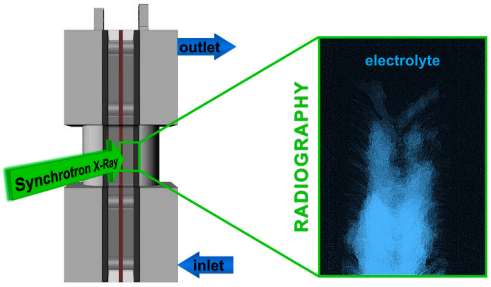

ARTICLE INFO

Keywords:
Synchrotron X-ray visualization
Electrolyte distribution
Vanadium redox flow battery
Carbon felt
Compression
Flow field

ABSTRACT

A porous carbon electrode fully saturated with electrolyte is one crucial aspect of vanadium redox flow battery efficiency. It determines the electrochemically active surface area, provides more active sites for the reaction during operation, and prevents local degradation due to inhomogeneities in electrolyte distribution. We investigate the electrolyte invasion and distribution at open-circuit potential in heat-treated carbon felt electrodes at varying compression ratios and flow field configurations, using synchrotron X-ray radiography. The quantitative analysis yields time-resolved saturation values of the injection and resolves local changes in saturation to detect areas of lower electrolyte accessibility. Compression ratios of 50% and above lead to a high electrode utilization with more than 97% saturation over the felt thickness. In contrast, carbon felts at 25% and 17% compression only reach 49% and 15% saturation near the flow fields. However, increasing the flow velocity after the injection causes the boundary area next to the flow field to fill even at low compressions. This area is especially critical for the electrode utilization since it is invaded after the bulk. Depending on the compression level, it does not reach full saturation.

* Corresponding author. Karlsruhe Institute of Technology, Helmholtz Institute Ulm, Helmholtzstraße 11, 89081, Ulm, Germany.
E-mail address: roswitha.zeis@kit.edu (R. Zeis).

https://doi.org/10.1016/j.jpowsour.2021.229660
Received 5 October 2020; Received in revised form 3 February 2021; Accepted 12 February 2021
Available online 23 February 2021

1. Introduction

To meet growing energy demand and simultaneously reduce greenhouse gas emissions, changing from fossil fuel-based energy production to sustainable and environmentally friendly renewable energy sources is strongly encouraged worldwide. Intermittent renewable energy from wind, solar, or hydropower plants necessitates energy storage devices to accommodate fluctuating power output [1–3]. Redox Flow Batteries (RFBs) are sustainable stationary energy storage devices that store excess energy via electrochemical redox reactions. The tunable design of RFBs allows an uncoupled adjustment of power and energy capacity and flexibility in their field of application, as they exhibit fast response times, comparatively low costs, high round-trip efficiencies, long cycle lives, and relatively low environmental impacts [3–6]. Developed in the late 1980s by Skyllas-Kazacos et al. [7], the Vanadium Redox Flow Battery (VRFB) is the most highly studied and commercially available type of RFB. The storage capability is based on two redox couples – V^{2+}/V^{3+} at the negative electrode and VO^{2+}/VO_2^+ at the positive electrode [4,8]. The VRFBS's overall performance is strongly influenced by the cell design, including the flow geometry [9] or the electrode compression [9–14], and by the types of components, such as the membrane [8,15], the electrolyte [16], and the electrodes [17–25].

Electrode compression causes opposing effects on the overall cell performance. Improved contact between the electrode and the current collector at higher compression ratios leads to higher voltage and energy efficiencies due to a lower contact resistance [11–14]. Conversely, the pressure drop increases at higher compression ratios, causing increased pumping losses and a drop in overall cell efficiency [9–11,14]. Additionally, the compression also strongly influences the internal electrode structure [12,14,26,27]. Jervis et al. used X-ray μ-CT to thoroughly analyze the effect of electrode compression on dry carbon felts [26]. They observed a non-linear compression and an increased directionality of the fibers at higher compressions. A spatially resolved analysis of the samples showed boundary effects, such as a lower porosity at the core and close to the sample holder's piston. These findings are important, as the electrode structure is a major factor in electrolyte distribution.

The redox reactions of the VRFB occur on the carbon electrodes' surface. It is essential to achieve a uniform electrolyte distribution and a thorough wetting of the electrodes to optimize the active species' mass transport and maximize the number of reaction sites, which benefits the system's overall efficiency [28,29]. However, the remaining air bubbles in the electrodes prevent an ideal mass transport, provoke undesired electrochemical reactions during operation, and accelerate electrode degradation in these areas [30]. Taking a closer look at the electrolyte flow can help us understand one crucial aspect of the overall VRFB performance. Ghimire et al. [11] used an innovative approach to resolve the flow distribution at different compressions locally. A segmented cell design allowed them to track the state of charge of the individual segments and locally resolve the discharging process. They concluded that 25% is the ideal compression ratio for a good VRFB performance since the deduced flow distribution was inhomogeneous for more strongly compressed carbon felts. Visualization techniques can track the electrolyte distribution and electrolyte transport mechanism in the electrodes directly [31]. Inspired by the advances in the three-dimensional visualization of fuel cells [32–36], the interest in X-ray visualization techniques to study electrochemical devices has grown tremendously in recent years [37,38]. X-rays can penetrate optically opaque materials and thus visualize the enclosed cells' electrode structures. This tool provides a relatively simple and non-destructive method of examining electrochemical devices with high spatial and temporal resolution. X-ray radiography and tomography have established themselves as a suitable visualization technique for VRFBs, while also providing input for modeling and simulations concerning pore size distributions or transport properties [17,27,39–41].

In addition to the visualization of structural changes in dry carbon electrodes [26,29,42], X-ray radiography and tomography can be applied to trace the electrolyte flow path, including possible hindrances, during the cell operation. In 2016, Jervis et al. [43] presented a cylindrical miniature flow cell that could resolve the carbon material, the static electrolyte, and air residues. Tariq et al. [30] used time-resolved X-ray μ-CT to visualize the imbibition of vanadium electrolyte into dry carbon paper electrodes. They reported a non-uniform progression front with an invasion mechanism of node-to-node filling, followed by the formation of so-called 'highway' channels as preferred electrolyte pathways. Adding to this work, Bevilacqua et al. [10] studied the electrolyte invasion of the vanadium electrolyte in the four oxidation states of a VRFB and showed that the type of vanadium species influences the saturation. Furthermore, this study revealed that a thermal pretreatment of the electrodes strongly enhances the electrode wetting and that electrode compression influences the saturation and the pressure drop. A subsequent study by Gebhard et al. [44] complemented these results by investigating the invasion percolation behavior of water, diluted sulfuric acid, and vanadium electrolyte into pristine and heat-treated carbon felts.

Our previous study [45] presented a novel VRFB design for X-ray visualization experiments with ample flexibility that enables the use of different materials, compression ratios, and flow geometries, as well as cell operation. The study reported the first experiments with synchrotron X-ray visualization of a VRFB under potential control, highlighting the changes in saturation during cyclic voltammetry measurements and at a constant negative potential. It was found that the hydrogen evolution and carbon corrosion side reactions during the electrode cycling led to a decrease in saturation that correlates with the respective current response.

For the first time, the herein presented work spatially resolves the vanadium electrolyte injection process into heat-treated carbon felt electrodes, quantifying the electrolyte saturation of specific parts of the carbon felt during the electrolyte invasion and propagation. We specifically focus on the interface between the flow field and the electrode, where we expect significant deviations from the bulk electrode's flow profile. Additionally, we investigate the influence of technically relevant aspects, such as the compression ratio, the flow field design, and an increased flow velocity. Using the previously presented in-house built cell, we can investigate commercial carbon felt electrodes of suitable size and observe manufacturing features. X-ray radiograms were conducted at a synchrotron facility, enabling a high temporal and spatial resolution of the dynamic processes due to a high photon flux. To spatially resolve the wetting behavior, the radiograms are divided into slices ranging from the flow field to the membrane. A time-resolved quantitative analysis is performed to display local electrolyte filling variations. In addition to qualitative descriptions of the processes, quantitative data are presented to compare the varying parameters' influence on the invasion and wetting behavior. By taking a closer look at the electrolyte distribution in VRFB electrodes, this study contributes fundamental results for one aspect of the overall VRFB performance.

2. Materials and methods

2.1. Electrode materials and vanadium electrolyte

The carbon electrode materials used for this study are graphitized Rayon-based carbon felts (SIGRACELL® GFA 6 EA) with a nominal thickness of 6 mm from SGL CARBON (Meitingen, Germany). They are manufactured by bonding two felts (3 mm thickness each) together, which creates a seam in the middle of the electrode, as highlighted in Fig. 1 (a). The disordered fiber arrangement, displayed in Fig. 1 (b), and the high porosity of 95% [46] cause the electrode material to be soft and compressible. In this study, the carbon felt electrodes were cut to 80 mm × 8 mm to fit the dimensions of the synchrotron cell built in-house [45] and compressed by ratios of 17%, 25%, 50% or 75% during the experiments by fitting the respective frame to control the thickness. All carbon felts were pretreated in a muffle furnace in an air atmosphere, applying a

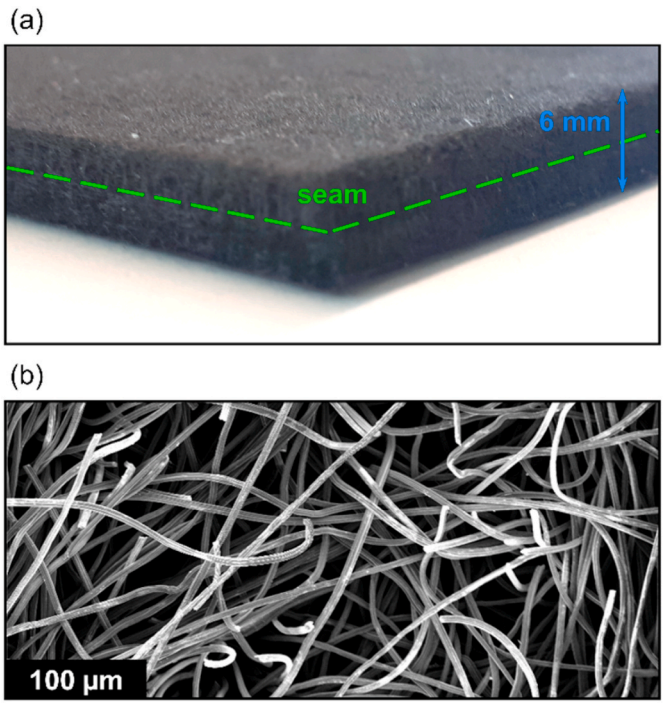

Fig. 1. (a) Photograph of the commercial SIGRACELL® GFA 6 EA carbon felt, highlighting the nominal thickness of 6 mm and the seam from manufacturing. (b) SEM image of the disordered fiber arrangement in the carbon felt taken at an acceleration voltage of 3.00 kV using an in-lens detector.

heating rate of 400 °C per hour for 1 h and a constant temperature of 400 °C for 25 h to enhance their wettability and introduce functional groups on the carbon surface [19,47,48].

The vanadium electrolyte for all experiments was prepared by dissolving 0.1 M $VOSO_4 \cdot 5\ H_2O$ (chemically pure, GfE) in 2 M H_2SO_4 (SUPRAPUR®, MERCK, diluted with purified Milli-Q water (18.2 MΩ cm)). The electrolyte was purged with nitrogen gas and subsequently transferred to a syringe before each experiment to remove atmospheric air.

2.2. Synchrotron setup

The X-ray radiograms and tomograms were captured at the Biomedical Imaging and Therapy Bending Magnet (BMIT-ID) 05ID-2 beamline at the Canadian Light Source Inc. (Saskatoon, Saskatchewan, Canada) [49]. The settings were identical to our previous publication [45], generating high-intensity monochromatic synchrotron radiation with an energy of 30 keV. Ten dark-field images (beam shutter closed) and ten flat-field images (beam shutter opened, no sample in beam path) were recorded before and after each radiography scan. The X-ray attenuation coefficient of the vanadium electrolyte at the given beam energy of 30 keV was calculated using a calibration device with several defined electrolyte thicknesses, as described in a previous publication ($\mu = 0.554\ cm^{-1}$ with $R^2 = 0.9999$) [45].

2.3. Standard measurement setup and experimental procedure

The standard measurement setup is based on a novel synchrotron cell (Fig. 2), which is developed in-house and enables the visualization of the electrolyte flow in a VRFB setup using X-ray radiography and tomography. The design and possible applications have been outlined in detail in our previous publication [45]. Three types of flow fields were applied to study flow-by (serpentine or interdigitated flow field) and flow-through (flat flow field) behavior, and frames of different thicknesses were used to vary the compression ratio of the electrodes

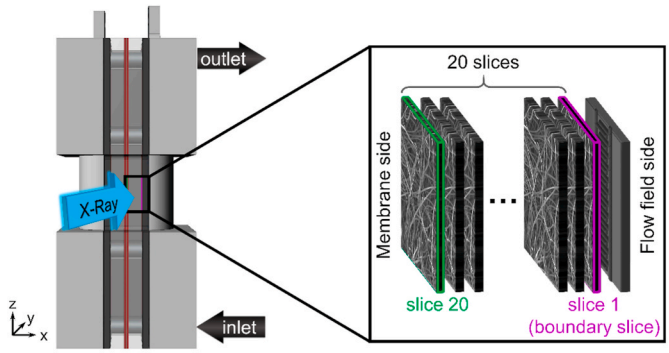

Fig. 2. Schematic synchrotron cell setup including end plates, flow fields, frames surrounding the carbon felt electrodes, gaskets, and the membrane. The electrolyte is injected on the bottom right and exits the right-hand electrode at the top right. The magnification explains how the images were divided into 20 slices to resolve the electrolyte injection and distribution spatially. This study's primary focus is the boundary slice next to the flow field (slice 1).

(compressed by 17%, 25%, 50% or 75%). The syringe was placed in a syringe pump (LA-100 by LANDGRAF LABORSYSTEME HLL, Langenhagen, Germany) to control the electrolyte's flow velocity. A NAFION® N117 membrane with a thickness of 178 µm separated the half-cells, and the same conditions (compression ratio and flow field) were applied to both electrodes of the cell.

For this study, we concluded six sets of measurements with varying compression ratios and flow fields according to the previously described procedure [45], including an *injection* process at 500 µL min^{-1} and a *flow* period at a flow rate of 30 mL min^{-1}. In all sets, we focused on the right-hand electrode, which is the first to be invaded by the electrolyte. The electrolyte is pumped into the bottom and exits the electrode through the outlet at the top before entering the second electrode on the left-hand side. The *injection* and *flow* procedures were performed at open-circuit potential. The radiograms were obtained to capture the electrolyte invasion's characteristics and flow inside the electrode. The term final radiogram corresponds to the average of the last 10 images in a radiography recording. Additionally, the saturation can be quantified by applying the Beer-Lambert law on the radiograms [32].

2.4. Data processing

The data processing of the radiograms was performed analogously to the previous publication on synchrotron X-ray radiography and tomography of VRFBs [45]. All images were dark-field-corrected, and the beam intensity decay was taken into account by applying a correction factor, as previously described by Hinebaugh et al. [50]. To determine the beam decay correction factor at a specific timestamp during the experiment, we assumed a linear decrease from the initial value of $f_1 = 1$. The adapted Beer-Lambert law was applied, as previously described by Ge et al. [32], and adopted by Eifert et al. [45] to calculate the electrolyte saturation of the carbon felts. Depending on the type of background in the calculation, this method can be utilized to compare the wet cell to a dry background to determine the absolute amount of electrolyte, e.g. after the *injection* process, or to describe changes in electrolyte saturation compared to a wet cell, e.g. after the *flow* period.

Spatial resolution of electrolyte saturation – For a more detailed study on the local electrolyte saturation, we divided each radiogram of the carbon felt electrode into 20 vertical slices (see Fig. 2) ranging from the boundary slice at the flow field on the right side (slice 1) to the membrane side (slice 20). Since the electrodes differ in their theoretical thicknesses due to the compression, we introduced relative thicknesses for a better comparison, with each slice corresponding to a relative thickness of 5%. This study spatially resolves the electrolyte invasion and flow for the whole thickness of the electrode but mainly focuses on

the boundary slice next to the flow field.

Time-resolved analysis – The starting point of the time-resolved analysis of the electrolyte *injection* process was set to 10 s (250 frames, frame rate of 25 fps) before a distinct increase in saturation could be observed. To achieve a more detailed display of the interesting section of each measurement, we only present the values up to the final plateau in saturation. The measurement continued after this point but showed no deviation from the respective constant saturation value.

3. Results and discussion

3.1. Injection experiment

The first part of this study deals with the vanadium electrolyte injection into dry carbon felts. We used a syringe pump to inject the electrolyte into the flow field with a flux of 500 μL min^{-1} without potential control. The electrolyte directly invades the carbon felt electrode at the bottom instead of following the channels of the flow field. This unexpected pathway can be ascribed to the higher wettability of the activated carbon felt electrode, which leads to electrolyte wicking, as previously shown in a study by Bevilacqua et al. [10]. Our study focuses explicitly on spatially resolving the carbon felt electrode's electrolyte saturation and thereby analyzing the wetting close to the flow fields in detail.

3.1.1. Influence of compression on the spatially resolved electrolyte saturation

X-ray radiograms of the *injection* at compressions of 17%, 25%, 50%, and 75% were recorded to investigate the influence of electrode compression on the wetting behavior and boundary effects. As presented in Fig. 3 (a), the radiograms were divided into 20 slices parallel to the interdigitated flow field with a relative thickness of 5% to locally resolve the electrolyte distribution. For all compression ratios, the local electrolyte saturation of these slices was calculated and is depicted in Fig. 3 (b). For clarity, the saturation is displayed at the mean relative thickness of each slice. For example, the first slice ranges from 0% to 5% in relative thickness, and the respective saturation value is shown at the mean value of 2.5%. In addition, the final radiogram of the *injection* procedure is displayed in Fig. 3 (c) and visualizes the electrolyte distribution in the half-cell for each compression ratio.

Overall, the final electrolyte saturation after the injection increases with higher electrodes' compression until it reaches more than 96% for compressions of 50% and above. However, the saturation is not uniform over the whole electrode thickness, and boundary effects need to be considered during the electrolyte injection. The carbon felt slice's saturation closest to the flow field (slice 1, 0%–5% relative thickness) strongly depends on the compression ratio and reaches only 15% for the least compressed felt and nearly 97% for compressions of 50% and higher. This issue is also visible in the radiograms, which display a small amount of electrolyte next to the flow field at a compression of 17% and a high saturation in this region for higher compressions. Moreover, the electrolyte invades the flow field at compression ratios above 50%, whereas the flow channels remain dry at lower compression. The low saturation at the flow field can be overcome by a higher flux, as explained further below. The significant drop in saturation close to 100% relative thickness (membrane side) can be attributed to the membrane itself, as visible in each sample's radiogram. For 25% compression and higher, the electrolyte saturation only strongly deviates at the flow field side and where the membrane is located. The small decrease in saturation at 40% relative thickness for 25%

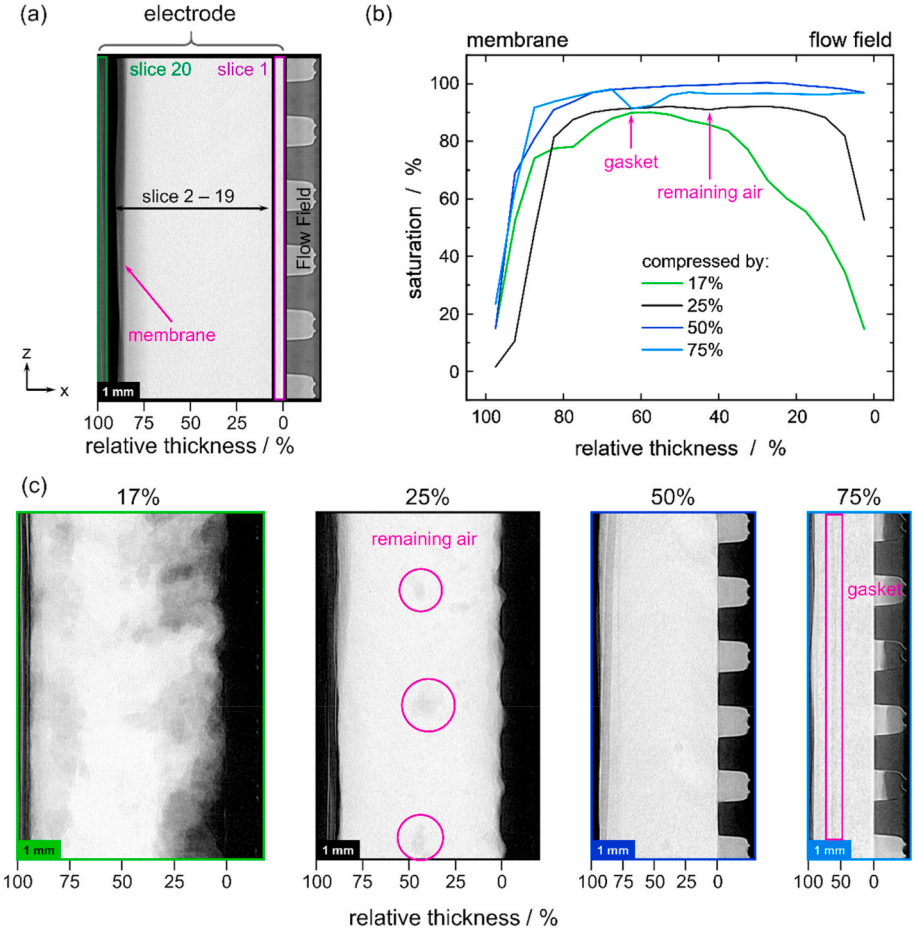

Fig. 3. (a) X-ray radiogram of a dry carbon felt electrode, depicting the 20 slices to resolve the electrolyte distribution spatially. (b) Calculated saturation of the carbon felt electrodes with vanadium electrolyte at different compression ratios after the electrolyte *injection* procedure (interdigitated flow field for all setups). The saturation was determined for 20 slices parallel to the flow field, ranging from the flow field (0% relative thickness, slice 1) up to the theoretical maximum thickness of the compressed felt (100% relative thickness, slice 20) and include the membrane. (c) X-ray radiograms of the electrolyte in the carbon felts after the *injection* procedure for the different compression ratios. The membrane is on the left and the flow field on the right side for each image. Only the difference between the dry and the wet half-cell is shown, resulting in a greyscale image of the electrolyte. The remaining air at 25% compression and the gasket at 75% compression are highlighted. The flow field channels are only filled at 50% and 75% compression.

compression is visible as slightly darker shaded regions in the radiogram and can be attributed to unfilled areas with trapped air bubbles. As explained previously, the SIGRACELL® GFA 6 EA felts are manufactured by bonding two felts (3 mm thickness each) together. This feature creates a seam in the middle of the electrode with smaller pore sizes, which influence the wetting/injection in this region. Therefore, the small deviation in saturation in this part of the felt is caused by reduced accessibility for the electrolyte close to the seam leading to residual air. Furthermore, a small saturation decrease at a relative thickness of 60% is observed for the highest compression of 75%, and is also visible in the radiogram in Fig. 3 (c) as a vertical grey line (highlighted with a purple frame). This observation can be attributed to a shift of the membrane gasket between the recording of the dry background image and the final wet radiogram, which leads to an artifact in the data processing.

In summary, this section shows that the electrolyte distribution at the end of the *injection* experiment, the final saturation, and the number of air bubbles strongly depends on the compression ratio. Furthermore, boundary effects are observed in the final radiograms, which affect the electrolyte injection of the carbon felt electrodes. This aspect is crucial for stacked electrodes with several boundaries, such as a carbon paper stack, since the electrolyte filling might be hindered. The section shows that the boundary effects can be mostly overcome by compressing the flow felts. However, since higher compression decreases the electrolyte's permeability and diffusivity [40], these boundary effects need to be considered in VRFB applications.

3.1.2. *Time-resolved analysis of the injection at different compression levels*

The importance of boundary effects is further emphasized by the time-resolved evaluation of the *injection* experiment, presented in Fig. 4. Representative radiograms at specific time stamps are depicted in Fig. 4 (a) and show that the compression strongly influences how fast and in which manner the electrolyte fills the carbon felt electrode. Furthermore, the quantitative data in Fig. 4 depicts the increase of saturation with time for the slice with the fastest imbibition (Fig. 4 (b)) and the slice at the boundary to the flow field (0%–5% relative thickness, Fig. 4 (c)) for each compression ratio, respectively.

Qualitative, time-resolved analysis of the injection process – For the compressions of 50% and below, the injection starts from the bottom left part of the half-cell (membrane side) and expands slowly upwards (z direction) and sideways (x direction) to the flow field, displaying the previously described phenomenon of fingering [10] in the top images of Fig. 4 (a). The electrolyte first establishes a path to the top of the field of view before spreading sideways to fill the rest of the carbon felt. This effect was explained by Tariq et al. with the establishment of so-called 'highway' channels [30], which are created by a node-to-node transport through the carbon felt before the invasion of adjacent smaller pores similar to capillary fingering. These 'highways' to the top of the field of view can be described as a preferred bypass route for the electrolyte and therefore cause other regions in the flow path to remain unfilled. For the less compressed carbon felts in this study, either one or two 'highway' channels are established next to the aforementioned seam of the carbon felt during the injection. This provides more evidence, that the seam of the carbon felt is not easily saturated and that a higher pressure is required to fill this region at low compressions. The subsequent lateral movement (x direction) of the electrolyte towards the flow field seems to follow the fiber alignment, since the compression leads to a tilt in the fiber alignment on both sides of the seam. Such a displacement of the carbon fibers under compression was also previously observed by Jervis et al. [26] and Xiao et al. [40]. As highlighted in Fig. 5, a higher compression ratio causes a steeper tilt angle and influences the wetting behavior. In the case of 50% and 75% compression, the fibers are tilted in the opposite direction due to the cell assembly.

At the highest compression ratio of 75%, the invasion pattern shows similarities to the other samples, but the imbibition proceeds more homogeneously via an invasion front over the whole thickness of the felt instead of forming 'highway' channels. Still, the filling process follows the single carbon fibers' tilted alignment.

In conclusion, the qualitative, time-resolved analysis of the invasion process shows that the invasion pattern depends on the level of compression and displays similarities in establishing 'highway' channels

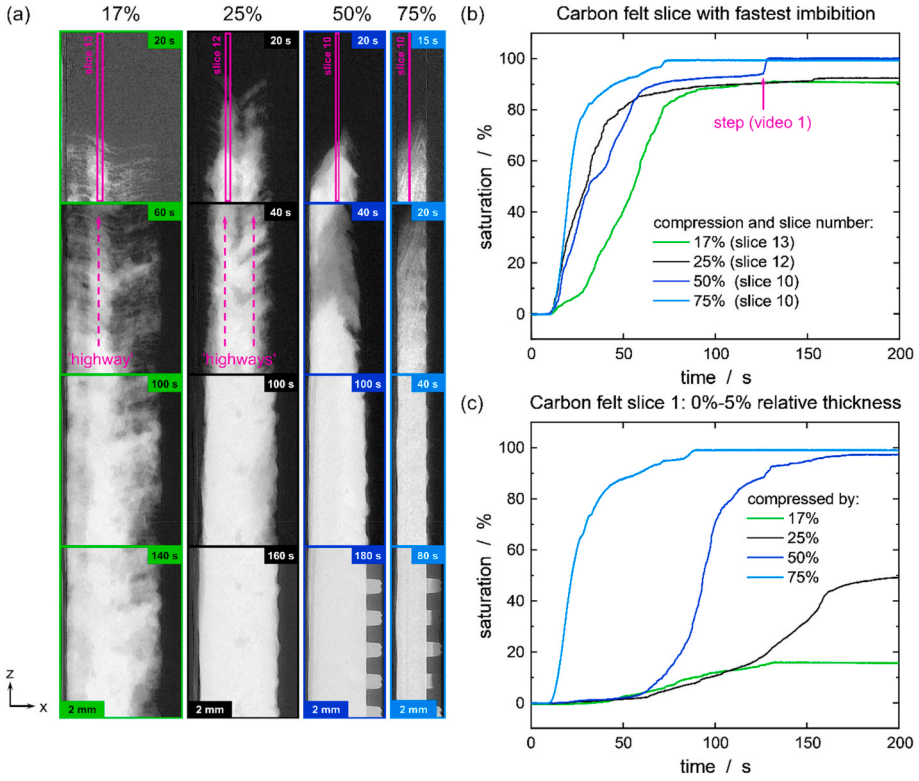

Fig. 4. (a) X-ray radiograms of the vanadium electrolyte in the carbon felts at specific points in time during the *injection*. The light areas correspond to the electrolyte, and the purple-framed sections represent the slices with the fastest imbibition. (b) Time-resolved saturation of the slice with the fastest imbibition for each carbon felt electrode during the *injection* process. The setup includes an interdigitated flow field for all samples, but different carbon felt compression ratios. The step-like increase in saturation at 50% compression is highlighted. (c) Time-resolved saturation of the boundary slice (slice 1, closest to flow field) of the carbon felt electrodes. (For interpretation of the references to color in this figure legend, the reader is referred to the Web version of this article.)

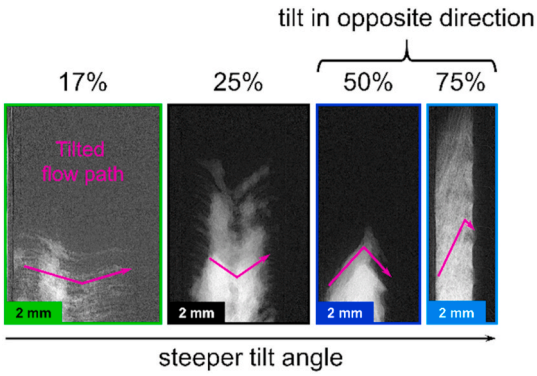

Fig. 5. X-ray radiograms of the vanadium electrolyte in the carbon felts after 20 s. The light areas correspond to the electrolyte, and the purple lines highlight the steeper tilt angle of the flow path at increasing compression ratio due to the fiber alignment. The flow path's tilt is in the opposite direction for 50% and 75% compression due to the cell assembly. (For interpretation of the references to color in this figure legend, the reader is referred to the Web version of this article.)

and spreading laterally along the tilted fibers. However, the cell assembly also influences the infiltration since it dictates how the carbon felt electrode reacts to the applied compression, e.g. how the fibers align and how strongly they are tilted.

Time-resolved saturation in the bulk of the carbon felt – Fig. 4 (b) displays the time-resolved saturation of the slices with the fastest imbibition for all four compression ratios. For each compression, this slice is located close to the center of the sample (see Fig. 4 (a)), and it is part of the 'highway' channel if one exists. This slice and the slice closest to the flow field represent the two extreme cases with the fastest and the slowest electrolyte invasion, respectively. Thus, all other slices exhibited an injection speed between these two examples and were not analyzed further. The linear part of the time-resolved saturation of the slice with the fastest imbibition was determined by eye, and a rate was calculated to compare the injection speed at different compression ratios. Using the lowest compression as reference, the rate is 1.45, 1.53, and 3.90 times higher at 25%, 50%, and 75% compression, respectively. Thus, the injection proceeds quicker when the felt is more compressed. As shown in previous studies [10,39], larger pores collapse at higher compression ratios, which reduces the mean pore diameter and thus requires higher pressures to invade the carbon felt electrode. Once this initial pressure before imbibition is overcome, the electrolyte floods the carbon felt and expands quickly to the electrode's top. The radiograms in the second row of Fig. 4 (a) show that the top of the field of view is already reached after 20 s at the highest compression of 75%, whereas it takes around 40 s at 50% and 25% compression and 60 s at the lowest compression of 17%.

Furthermore, it can be concluded from the radiograms in the bottom two rows that the lateral spreading of the electrolyte proceeds slower in less compressed felts. In addition to the differences in invasion speed, the slices with the fastest injection final saturation vary slightly but reach a high level in all samples. Above 50% compression, the saturation gets close to 100%, whereas the less compressed felts reach saturation values of 92% and 90% for the respective slices at 25% and 17% compression. In the case of 50% compression, the carbon felt slice with the fastest invasion first reaches a constant saturation of 80% after 70 s, followed by a step-like increase to a saturation plateau of close to 100% (highlighted in Fig. 4 (b)). Before this increase, a shielding effect of smaller pores with a higher entry pressure surrounding large pores might render the larger pores of the carbon felt electrode inaccessible, and as a result, the saturation stays at a constant level [26]. However, as more electrolyte is injected, the pressure increases until the small surrounding pores become accessible after 125 s and are immediately filled with electrolyte, leading to the subsequent filling of the shielded large pores. This process is expressed by a step-like increase in saturation, as previously explained by Banerjee et al. [17]. From a time-resolved animation of the process, it can be distinguished that a new part of the felt is accessed by the electrolyte at this point (see Video 1 in supporting information).

Supplementary data to this article can be found online at https://doi.org/10.1016/j.jpowsour.2021.229660

Overall, the analysis of the electrolyte invasion process of the slice with the fastest imbibition revealed that this slice is typically located in the 'highway' channels. Its invasion speed depends on the compression level, showing the fastest filling of the carbon felt slice at the highest compression ratio of 75%. Moreover, jumps in saturation can be observed if specific areas are initially not accessible.

Time-resolved electrolyte invasion at the flow field boundary – Close to the flow field, the invasion strongly depends on the carbon felt's compression ratio, as a lower compression leads to slower imbibition, and a lower final saturation of the carbon felt in this area. Furthermore, the injection in these boundary slices (Fig. 4 (c)) takes much longer compared to the previously presented invasion in the center of the electrodes (Fig. 4 (b)). For all compressions, a constant saturation is reached in the boundary slice before the end of the *injection* process, when the syringe pump is turned off. This saturation cannot be further increased without changing the flow rate, implying that a higher pressure is required to fill the remaining empty pores. At compressions of 75% and 50%, the saturation reaches 99% and 97%, respectively, which shows that the carbon felt is filled even at the boundary to the flow field.

In contrast, the saturation only amounts to 49% and 15% for the felt at 25% and 17% compression, respectively. The pressure of the flow field on the carbon felt electrodes is smaller for smaller compression ratios, and therefore, the contact between the electrode and the flow field is less pronounced, and the electrolyte avoids the pathways close to the hydrophobic flow field. Since the electrolyte does not entirely reach the flow field at 17% compression, no electrolyte invasion from the felt back into the flow field can be observed. This issue is especially crucial for the interdigitated flow field, where the electrolyte inlet and outlet are not directly connected. Thus, the electrolyte, which is pushed into the carbon felt from the inlet, needs to re-enter the flow field to reach the electrolyte outlet of the cell and allow for electrolyte circulation in a full-cell setup.

Similarly to the case at 17% compression, the bottom radiogram in Fig. 4 (a) shows that the flow field is not entirely saturated at 25% compression either but is slightly invaded by the electrolyte since the carbon felt electrode is pressed against the flow field more strongly and even intrudes it, as previously presented by Chang et al. [12]. At compressions of 50% and above, the interdigitated flow field's flow channels are filled during the *injection* process. However, due to the high electrode compression, the largest pores collapse [39], resulting in a higher entry pressure than the generally more hydrophobic flow fields.

In summary, this section shows that the boundary effects during the electrolyte invasion at low flow velocity strongly depend on the level of compression. At low compressions, the electrolyte preferably fills the bulk of the carbon felt electrode, and the area close to the flow field is only slightly invaded. In contrast, at compressions of 50% and above, the electrolyte invasion starts from the bottom, expands sideways, and even fills the flow fields, reaching close to 100% saturation in the boundary slice.

3.1.3. *Influence of the flow field configuration on the spatially resolved electrolyte saturation*

The influence of different flow fields on the spatially resolved saturation is small compared to the influence of compression, as displayed in Fig. 6 (a). Serpentine and interdigitated flow fields were applied as flow-by configurations, and a flat flow field was used to study flow-through behavior. A compression ratio of 25% was chosen for all samples in this section.

The saturation is similar over a wide range for all flow field

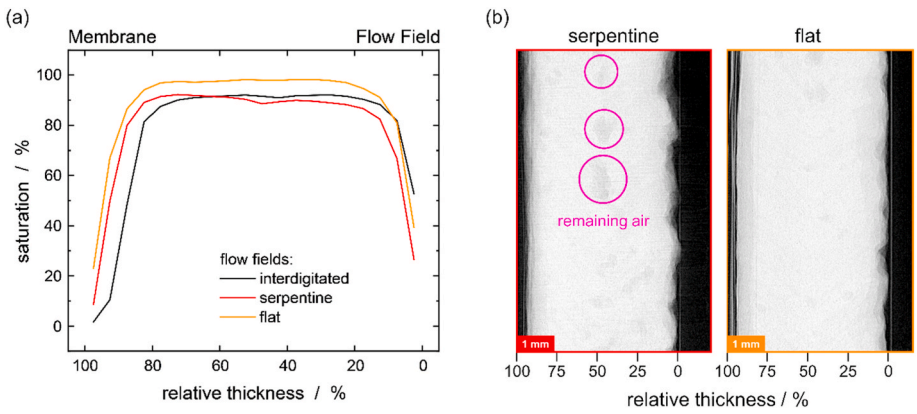

Fig. 6. (a) Calculated saturation of the carbon felt electrodes with vanadium electrolyte after the electrolyte *injection* procedure using different flow fields and 25% compression. The saturation was determined for 20 slices from the flow field (0% relative thickness) up to the theoretical maximum thickness of the compressed felt (100% relative thickness) and includes the membrane. (b) Visualization of the vanadium electrolyte in the carbon felts through X-ray radiography after the *injection* procedure for the serpentine and flat flow field. The interdigitated flow field setup at 25% compression is already presented in Fig. 3 (c). The light color corresponds to the electrolyte. (For interpretation of the references to color in this figure legend, the reader is referred to the Web version of this article.)

configurations and deviates specifically close to the flow field at low relative thickness and at the membrane. The flat flow field reaches the highest bulk saturation of 98%, but the serpentine and interdigitated flow fields still achieve high values of 90% and 92% saturation, respectively. However, all samples display lower electrolyte saturation close to the flow field (0%–5% relative thickness) with 39%, 27%, and 53% saturation for the flat, serpentine, and interdigitated flow field, respectively.

The final radiograms presented in Fig. 6 (b) for the serpentine and flat flow field resemble the previously presented electrolyte distribution with the interdigitated flow field (Fig. 3 (b)). Darker spots in the center of the felt show the presence of remaining air, which results in a drop of 1%–2% in saturation at the respective relative thickness for the serpentine and interdigitated flow field. In contrast, the electrolyte saturation with the flat flow field is more homogeneous and has no distinct drop in the electrode center. This observation can be explained by the presence of flow channels in the serpentine and the interdigitated flow field. Although the electrolyte does not fill these channels at this compression ratio in the presented field of view, they still enable the electrolyte to reduce the pressure drop by bypassing the felt and flowing through the less hydrophilic flow field channels.

Conversely, the flat flow field does not allow bypassing and therefore forces the electrolyte to fill smaller or less accessible pores, such as those close to the seam. Besides, this flat flow field feature also impedes the filling of the area close to the flow field since the electrolyte is faced by a flat surface and cannot invade any channels. At a low flow velocity, the channels' presence influences the electrolyte distribution, whereas, at a higher flow velocity, the pressure drop is significantly higher in the case of a flat flow field compared to flow fields with bypassing options [51]. Increasing the hydrophilicity of the flow fields by modification could improve the boundary region's filling. Instead of invading the electrode at the cell's inlet, the electrolyte could partially take the path through the flow fields and fill the boundary region directly from the flow field side.

3.1.4. *Time-resolved analysis of the injection with different flow field configurations*

As previously presented by Eifert et al. [45], the time-resolved invasion follows a similar pattern for all flow fields: establish 'highway' channels around the seam in the center of the felt and follow the fiber structure during the lateral spreading. To add to these results, Fig. 7 presents a quantitative analysis of the wetting with spatially resolved saturation values during the *injection* procedure for all flow field types in time intervals of 15 s.

All three flow field configurations show similarities in the invasion process. The seam from the manufacturing procedure (at ca. 50% relative thickness) severely impacts the *injection* process since the 'highway' channels establish around it. Furthermore, the invasion tends to proceed faster at the beginning of the process and slows down when the carbon felt electrode is nearly filled, which agrees with previous findings from Bevilacqua et al. [10].

For the interdigitated flow field, the seam is located at ca. 50% relative thickness and the drop in saturation is more pronounced at the beginning of the *injection* process but can still be observed in the spatially resolved saturation of the final radiogram in Fig. 6 (a). Between 30% and 70% relative thickness, the carbon felt becomes saturated faster and reaches a constant saturation after 90 s, whereas the boundary areas fill more slowly than the center. It can be observed that the saturation next to the flow field increases faster during the later stages of the measurement since the distance between the time-resolved curves increases. This effect can be attributed to new pores that become accessible and filled immediately, leading to a sudden jump in electrolyte saturation, as Jervis et al. explained with a shielding effect of small pores [26]. This phenomenon could be attributed to Haines instabilities, which are likely to appear in soft porous systems like carbon felts when fluid is suddenly redistributed [52].

In contrast, this behavior is not observed for the serpentine flow field, and the distance between the time-resolved saturation curves decreases steadily, meaning the filling process slows down with time. Furthermore, a constant level of electrolyte saturation is reached after

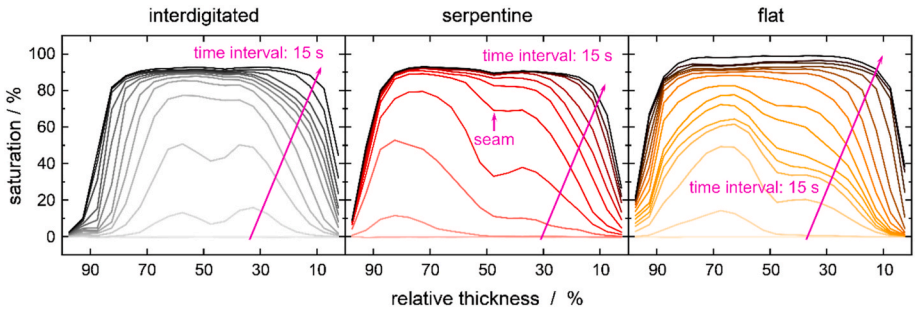

Fig. 7. Time-resolved, calculated saturation of the carbon felt electrodes with vanadium electrolyte during the *injection* process using an interdigitated, serpentine and flat flow field at 25% compression. The saturation was determined for 20 slices from the flow field (0% relative thickness) up to the theoretical maximum thickness of the compressed felt (100% relative thickness) and includes the membrane. The time interval between the presented saturation curves is 15 s. The seam is marked in the case of the serpentine flow field. In the beginning, its impact is visual for all cases.

60 s on the left side of the carbon felt seam, whereas the right side next to the flow field is filled more slowly since the electrolyte is preferably transferred from the membrane side. Similar to the interdigitated flow field, the drop in saturation close to 50% relative thickness can be distinguished from the beginning of the injection and up to the final radiogram in the case of the serpentine flow field.

As described previously, the lower saturation in the center of the felt cannot be observed after the *injection* procedure using the flat flow field. However, at the beginning of the injection, the drop is distinguishable since the adjacent regions are filled faster than the center. The injection behavior is similar to the serpentine flow field, displaying a faster filling on the left side due to a 'highway' channel and the subsequent filling of the right side, which can mostly be ascribed to electrolyte transport across the seam that could be observed in the radiograms during the *injection* process (see Video 2 in supporting information). The carbon felt filling is slower, and a constant saturation is only reached after 195 s, compared to both flow-by configurations, where a constant saturation is reached after 165 s (interdigitated) and 150 s (serpentine). A sudden further increase in saturation to the final level can be observed in the center region between 30% and 80% relative thickness, which can also be explained by the shielding effect and Haines instabilities as described above.

Supplementary data to this article can be found online at https://doi.org/10.1016/j.jpowsour.2021.229660

In summary, this section shows that the flow fields' influence on the *injection* process is small and that all flow field configurations show a similar invasion pattern. Overall, the bulk of the carbon felt electrodes is filled faster than the boundary regions. However, the seam area in the center of the felt is invaded later in the *injection* process, leading to a drop in the spatially resolved saturation that only levels off for the flat flow field. In electrolyte saturation, sudden jumps can be observed for two samples and are ascribed to the shielding effect, previously described by Jervis et al. [26].

3.2. Flow procedure

As previously mentioned, all samples reach a saturation plateau near the flow field during the *injection* but do not reach a saturation of 100%, as observed in the center area. Thus, higher entry pressures are required to fill these regions, which can be achieved by increasing the flow velocity. Following the *injection* procedure (500 µL min^{-1}), we included a *flow* period, during which the electrolyte was pumped with a flow rate of 30 mL min^{-1} at open-circuit potential. Fig. 8 (a) and (b) present the spatially resolved changes in saturation between the two subsequent procedures for different compression ratios and flow fields, respectively. A positive change in saturation corresponds to additional electrolyte invasion, whereas a value of 0% implies no changes in the amount of electrolyte in the respective slice. Negative values can be attributed to the redistribution of electrolyte inside the carbon felt, leading to new air pockets, which locally reduce the saturation.

Influence of compression on the spatially resolved change in saturation during the flow period – For all measurements, the most significant change in saturation at the flow field boundary is observed for the lowest compression of 17%. Since the carbon felt was not filled in this region after the *injection* process, the higher flow velocity leads to a substantial increase in the saturation of more than 50% by overcoming the inlet pressure of a new set of pores. Furthermore, the center region of the carbon felt electrode (ca. 30%–80% relative thickness) also exhibits a change in saturation of 3%–10%, leading to an overall increase in the electrolyte saturation after the *flow* period. The final radiogram in Fig. 8 (c) displays a homogeneous electrolyte distribution from the flow field side to the membrane, with several trapped air bubbles spread over the entire visualized section of the carbon felt electrode. The vanadium electrolyte partially invades the interdigitated flow field's channels on the right side. However, they are not filled completely.

The higher compression of 25% shows nearly no changes in the bulk saturation and even a few slices with an adverse change in saturation due to the redistribution of electrolyte, accompanied by the relocation of air bubbles. However, an increase of 15% at the flow field and up to 80% at the membrane can be observed. The final radiogram at this compression in Fig. 8 (c) shows that the vast increase in saturation at the membrane can be attributed to the filling of the second carbon felt electrode in the setup, located on the left side of the membrane. During the *injection* period, the electrolyte is only injected into the right-hand electrode, so the spatially resolved saturation increases in this electrode. The lower saturation at high relative thickness after the injection can be ascribed to the membrane and the unfilled second electrode. During the *flow* period, the electrolyte reaches the left-hand carbon felt, and as a result, the electrolyte saturation increases strongly at high relative thickness.

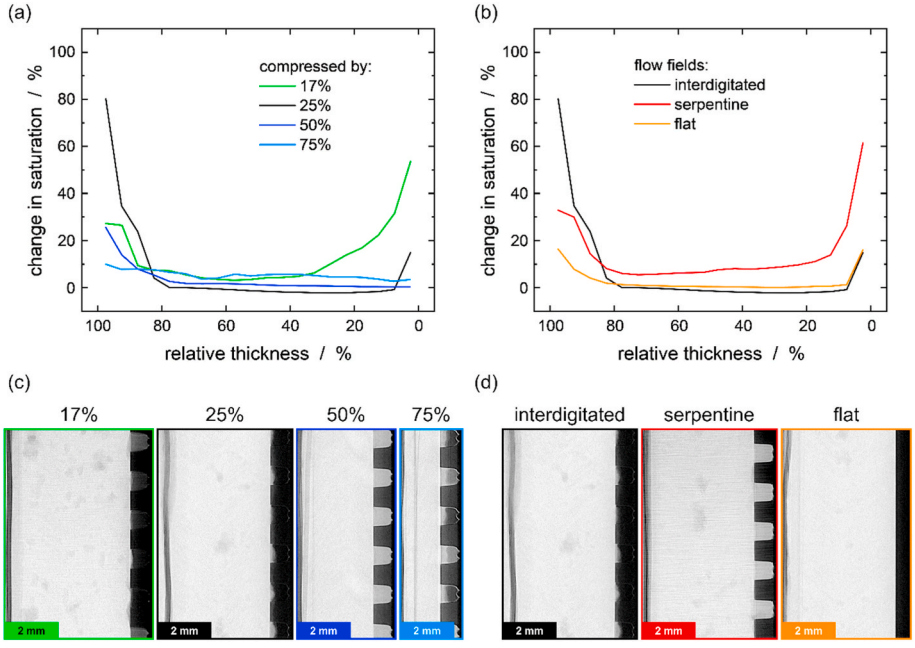

Fig. 8. Top: Change in electrolyte saturation of the carbon felt electrodes between the end of the *injection* procedure and the end of the *flow* period using (a) different compression ratios and an interdigitated flow field or (b) different flow fields and 25% compression. The saturation was determined for 20 slices from the flow field (0% relative thickness) up to the theoretical maximum thickness of the compressed felt (100% relative thickness) and includes the membrane. Bottom: Visualization of the final vanadium electrolyte distribution in the carbon felts through X-ray radiography after the *flow* procedure with (c) different compression ratios and an interdigitated flow field and (d) different flow fields at 25% compression. The light areas correspond to the electrolyte.

The electrolyte saturation changes at the higher compression ratios of 50% and 75% are only small and on a similar level over the whole thickness of the carbon felt electrodes. This observation is consistent with them after the *injection* since both samples were already highly saturated, even at the flow field boundary. The respective radiograms after the continuous flow, presented in Fig. 8 (c), still display a darker vertical line at 75% compression due to the shift of the membrane gasket and a dark feature at 50% compression, which can be attributed to a shift of the membrane itself. Furthermore, it was observed that in both cases, the interdigitated flow fields are invaded by the electrolyte in contrast to the lower compression ratios. The higher pressure inside the carbon felt can be explained by the higher compression ratio, which renders the bypass through the less hydrophilic flow fields more favorable.

Influence of the flow fields on the spatially resolved change in saturation during the flow period – Applying the flat flow field and a compression of 25%, the change in saturation is similar to the setup with the interdigitated flow field, as displayed in Fig. 8 (b). They only strongly differ on the left side of the investigated section since the membrane is located at nearly 100% relative thickness in the flat flow field. Therefore, the substantial increase due to the filling of the second carbon felt during the *flow* process is outside the field of view.

In contrast, the serpentine flow field setup shows an overall increase in the saturation of around 5%–10% in the center region (ranging from ca. 20%–80% relative thickness) and 61% at the flow field side. The serpentine flow field exhibits the lowest electrolyte saturation at the boundary after the *injection* procedure, and thus, most of these empty pores are filled in the subsequent *flow* period.

Furthermore, the serpentine flow field channels are now filled after the continuous flow at a higher flow rate (see Fig. 8 (d)), even though they exhibit lower hydrophilicity than the carbon felt electrode. Since the inlet and the outlet are directly connected, the electrolyte might use this bypass option to even out the pressure and prevent higher pressure drops. However, this option is impossible with the interdigitated flow field since the electrolyte has to pass through the carbon felt to reach the flow field outlet. Therefore, the electrolyte only partially invades the channels at this compression ratio, as displayed in Fig. 8 (d).

Overall, the higher electrolyte flow velocity during the *flow* period allows the electrolyte to enter the previously unfilled regions of the carbon felt since the entry pressure can be overcome in all samples. Independent of the type of flow field and the compression ratio, the boundary slice close to the flow field is filled during this process, and afterward, the saturation values remain nearly constant over the whole thickness of the felts. All of the radiograms in Fig. 8 (c) and (d) still show air residues close to the center of the samples, where the seam is located, even after increasing the flow velocity during the *flow* procedure. This issue must be considered when deciding on the flow velocity in industrial applications since remaining air bubbles can cause undesired electrochemical reactions and locally accelerate the electrode degradation, leading to decreased cycling life [30]. Since these results imply that the compression and the choice of flow field only slightly influence the final saturation of the carbon felts at higher flow velocity, other factors, such as increased pumping losses for higher compressions, should be strongly considered for the overall cell performance.

4. Conclusion

In this study, a VRFB built in-house was used to visualize the electrolyte injection and the electrolyte flow through heat-treated carbon felt electrodes via synchrotron X-ray imaging techniques. Flow-through (flat flow field) and flow-by (serpentine and interdigitated flow fields) configurations with various compression ratios were applied to examine the system design's effects on the electrolyte invasion and distribution. The local electrolyte saturation and boundary effects were investigated in detail. Furthermore, the injection was resolved over time by quantifying the electrolyte saturation in the carbon felt throughout the invasion.

It was observed that the wetting varies distinctly in the different parts of the carbon felt electrode after electrolyte injection. A decrease in saturation due to air residues mostly occurs in the center of the electrode, attributed to manufacturing features. Furthermore, the flow field's boundary region displays a lower saturation in all samples due to the electrolyte invasion pattern. This aspect is crucial for stacked electrodes with several boundaries since the electrolyte filling might be impeded. The electrolyte invasion follows a similar behavior, regardless of the type of flow field or the compression ratio. It expands in a fingering manner and establishes one or two 'highway' paths that reach the top of the field of view first and leave the rest of the carbon felt mostly unfilled. Afterward, the electrolyte follows the typically tilted fiber alignment and spreads sideways towards the flow fields. The time-resolved analysis revealed that the filling slows down over time and that a constant saturation is reached for all parts of the felt after the *injection* period. Sudden step-like increases were observed when the shielding effect of surrounding pores is overcome, and the adjacent pores are filled instantaneously.

For higher compression levels, the whole invasion process proceeds faster, and the steps mentioned earlier cannot be resolved Additionally, the carbon felts' saturation after injection also increases with the level of compression. Above 50% compression, the saturation reaches over 97% in all parts of the electrode, whereas only the bulk is sufficiently wetted at 25% and 17% compression, and the boundary slices only reach 49% and 15% saturation, respectively. The effect of different flow fields on the electrolyte invasion is small, with the only noticeable difference in the flow-through configuration of the flat flow field, which displays an overall higher saturation and a more homogeneous electrolyte distribution. However, increasing the flow velocity after the initial injection allows the electrolyte to overcome the entry pressure of unfilled pores and thus causes the boundary area at the flow field to fill up in all samples, only leaving behind a few air residues distributed throughout the electrode.

For the first time, this work spatially resolves the electrolyte invasion into carbon felt electrodes for VRFBs, thereby considering technically relevant aspects like the flow field configuration, the compression ratio, and the flow velocity. This work shows that electrolyte invasion through the porous electrode is a complex process. Only partially filled electrode areas decrease the wetted surface area and cause local degradation. In our experiment, a higher flow velocity is beneficial for the boundary regions but would be detrimental to the energy efficiency due to increased pumping losses. These findings in mind, subsequent experiments, could improve the wetting of the boundary regions to increase the active surface area and improve the overall efficiency of VRFBs.

Authors contribution

K. Köble: Design and conduct of experiments, formal analysis, data curation, draft writing. L. Eifert: Design and conduct of experiments, scientific discussion, linguistic support. N. Bevilacqua: Design and conduct of experiments, scientific discussion, linguistic support. K. Fahy: Conduct of experiments, scientific discussion, linguistic support. A. Bazylak: Scientific discussion, linguistic support, supervision, R. Zeis: Conceptualization, scientific discussion, linguistic support, supervision, funding.

Declaration of competing interest

The authors declare that they have no known competing financial interests or personal relationships that could have appeared to influence the work reported in this paper.

Acknowledgments

We gratefully acknowledge the Impuls-und Vernetzungsfonds der

Helmholtz Gesellschaft (Young Investigator Group project VH-NG-616) for the financial support and SGL Carbon for the supply of SIGRACELL® carbon felts. K.K. gratefully acknowledges financial support through a Kekulé Ph.D. fellowship by the Fonds der Chemischen Industrie (FCI). The authors also gratefully acknowledge funding support from the Natural Sciences and Engineering Research Council of Canada (NSERC) Discovery Grant Program and the Canada Research Chairs Program. This study was further supported by Sergey Gasilov, Denise Miller, Adam Webb, Ning Zhu, and the Biomedical Imaging and Therapy (BMIT) beamline staff.

The research described in this paper was performed at the Canadian Light Source, which is supported by the Canada Foundation for Innovation, Natural Sciences and Engineering Research Council of Canada, the University of Saskatchewan, the Government of Saskatchewan, Western Economic Diversification Canada, the National Research Council Canada, and the Canadian Institutes of Health Research.

This work contributes to the research performed at CELEST (Center for Electrochemical Energy Storage Ulm-Karlsruhe).

References

[1] B. Dunn, H. Kamath, J.-M. Tarascon, Electrical energy storage for the grid: a battery of choices, Science (80-.) 334 (2011) 928–935, https://doi.org/10.1126/science.1212741.

[2] M. Skyllas-Kazacos, M.H. Chakrabarti, S.A. Hajimolana, F.S. Mjalli, M. Saleem, Progress in flow battery research and development, J. Electrochem. Soc. 158 (2011), https://doi.org/10.1149/1.3599565. R55–R79.

[3] A.Z. Weber, M.M. Mench, J.P. Meyers, P.N. Ross, J.T. Gostick, Q. Liu, Redox flow batteries: a review, J. Appl. Electrochem. 41 (2011) 1137–1164, https://doi.org/10.1007/s10800-011-0348-2.

[4] K. Lourenssen, J. Williams, F. Ahmadpour, R. Clemmer, S. Tasnim, Vanadium redox flow batteries: a comprehensive review, J. Energy Storage. 25 (2019) 100844, https://doi.org/10.1016/j.est.2019.100844.

[5] P. Alotto, M. Guarnieri, F. Moro, Redox flow batteries for the storage of renewable energy: a review, Renew. Sustain. Energy Rev. 29 (2014) 325–335, https://doi.org/10.1016/j.rser.2013.08.001.

[6] C. Minke, T. Turek, Materials, system designs and modelling approaches in techno-economic assessment of all-vanadium redox flow batteries – a review, J. Power Sources 376 (2018) 66–81, https://doi.org/10.1016/j.jpowsour.2017.11.058.

[7] M. Skyllas-Kazacos, M. Rychcik, R.G. Robins, A.G. Fane, New all-vanadium redox flow cell, J. Electrochem. Soc. 133 (1986) 1057, https://doi.org/10.1149/1.2108706.

[8] Y. Shi, C. Eze, B. Xiong, W. He, H. Zhang, T.M. Lim, A. Ukil, J. Zhao, Recent development of membrane for vanadium redox flow battery applications: a review, Appl. Energy 238 (2019) 202–224, https://doi.org/10.1016/j.apenergy.2018.12.087.

[9] A. Bhattarai, N. Wai, R. Schweiss, A. Whitehead, T.M. Lim, H.H. Hng, Advanced porous electrodes with flow channels for vanadium redox flow battery, J. Power Sources 341 (2017) 83–90, https://doi.org/10.1016/j.jpowsour.2016.11.113.

[10] N. Bevilacqua, L. Eifert, R. Banerjee, K. Köble, T. Faragó, M. Zuber, A. Bazylak, R. Zeis, Visualization of electrolyte flow in vanadium redox flow batteries using synchrotron X-ray radiography and tomography – impact of electrolyte species and electrode compression, J. Power Sources 439 (2019) 227071, https://doi.org/10.1016/j.jpowsour.2019.227071.

[11] P.C. Ghimire, A. Bhattarai, R. Schweiss, G.G. Scherer, N. Wai, Q. Yan, A comprehensive study of electrode compression effects in all vanadium redox flow batteries including locally resolved measurements, Appl. Energy 230 (2018) 974–982, https://doi.org/10.1016/j.apenergy.2018.09.049.

[12] T.-C. Chang, J.-P. Zhang, Y.-K. Fuh, Electrical, mechanical and morphological properties of compressed carbon felt electrodes in vanadium redox flow battery, J. Power Sources 245 (2014) 66–75, https://doi.org/10.1016/j.jpowsour.2013.06.018.

[13] S.-K. Park, J. Shim, J.H. Yang, C.-S. Jin, B.S. Lee, Y.-S. Lee, K.-H. Shin, J.-D. Jeon, The influence of compressed carbon felt electrodes on the performance of a vanadium redox flow battery, Electrochim. Acta 116 (2014) 447–452, https://doi.org/10.1016/j.electacta.2013.11.073.

[14] L.D. Brown, T.P. Neville, R. Jervis, T.J. Mason, P.R. Shearing, D.J.L. Brett, The effect of felt compression on the performance and pressure drop of all-vanadium redox flow batteries, J. Energy Storage. 8 (2016) 91–98, https://doi.org/10.1016/j.est.2016.10.003.

[15] S.I. Hossain, M.A. Aziz, S. Shanmugam, Ultrahigh ion-selective and durable nafion-NdZr composite layer membranes for all-vanadium redox flow batteries, ACS Sustain. Chem. Eng. 8 (2020), https://doi.org/10.1021/acssuschemeng.9b06541, 1998–2007.

[16] M. Skyllas-Kazacos, L. Cao, M. Kazacos, N. Kausar, A. Mousa, Vanadium electrolyte studies for the vanadium redox battery-A review, ChemSusChem 9 (2016) 1521–1543, https://doi.org/10.1002/cssc.201600102.

[17] R. Banerjee, N. Bevilacqua, L. Eifert, R. Zeis, Characterization of carbon felt electrodes for vanadium redox flow batteries – a pore network modeling approach, J. Energy Storage. 21 (2019) 163–171, https://doi.org/10.1016/j.est.2018.11.014.

[18] A. Forner-Cuenca, F.R. Brushett, Engineering porous electrodes for next-generation redox flow batteries: recent progress and opportunities, Curr. Opin. Electrochem. 18 (2019) 113–122, https://doi.org/10.1016/j.coelec.2019.11.002.

[19] L. Eifert, R. Banerjee, Z. Jusys, R. Zeis, Characterization of carbon felt electrodes for vanadium redox flow batteries: impact of treatment methods, J. Electrochem. Soc. 165 (2018) A2577, https://doi.org/10.1149/2.0531811jes. –A2586.

[20] M. Schnucklake, L. Eifert, J. Schneider, R. Zeis, C. Roth, Porous N- and S-doped carbon–carbon composite electrodes by soft-templating for redox flow batteries, Beilstein J. Nanotechnol. 10 (2019) 1131–1139, https://doi.org/10.3762/bjnano.10.113.

[21] O. Nibel, S.M. Taylor, A. Pătru, E. Fabbri, L. Gubler, T.J. Schmidt, Performance of different carbon electrode materials: insights into stability and degradation under real vanadium redox flow battery operating conditions, J. Electrochem. Soc. 164 (2017) A1608–A1615, https://doi.org/10.1149/2.1081707jes.

[22] H.R. Jiang, W. Shyy, Y.X. Ren, R.H. Zhang, T.S. Zhao, A room-temperature activated graphite felt as the cost-effective, highly active and stable electrode for vanadium redox flow batteries, Appl. Energy 233–234 (2019) 544–553, https://doi.org/10.1016/j.apenergy.2018.10.059.

[23] A. Fetyan, J. Schneider, M. Schnucklake, G.A. El-Nagar, R. Banerjee, N. Bevilacqua, R. Zeis, C. Roth, Comparison of electrospun Carbon−Carbon composite and commercial felt for their activity and electrolyte utilization in vanadium redox flow batteries, ChemElectroChem 6 (2019) 130–135, https://doi.org/10.1002/celc.201801128.

[24] T. Liu, X. Li, H. Zhang, J. Chen, Progress on the electrode materials towards vanadium flow batteries (VFBs) with improved power density, J. Energy Chem. 27 (2018) 1292–1303, https://doi.org/10.1016/j.jechem.2018.07.003.

[25] T.X. Huong Le, M. Bechelany, M. Cretin, Carbon felt based-electrodes for energy and environmental applications: a review, Carbon N. Y. 122 (2017) 564–591, https://doi.org/10.1016/j.carbon.2017.06.078.

[26] R. Jervis, M.D.R. Kok, T.P. Neville, Q. Meyer, L.D. Brown, F. Iacoviello, J. T. Gostick, D.J.L. Brett, P.R. Shearing, In situ compression and X-ray computed tomography of flow battery electrodes, J. Energy Chem. 27 (2018) 1353–1361, https://doi.org/10.1016/j.jechem.2018.03.022.

[27] D. Emmel, J.D. Hofmann, T. Arlt, I. Manke, G.D. Wehinger, D. Schröder, Understanding the impact of compression on the active area of carbon felt electrodes for redox flow batteries, ACS Appl. Energy Mater. 3 (2020) 4384–4393, https://doi.org/10.1021/acsaem.0c00075.

[28] M.-A. Goulet, M. Skyllas-Kazacos, E. Kjeang, The importance of wetting in carbon paper electrodes for vanadium redox reactions, Carbon N. Y. 101 (2016) 390–398, https://doi.org/10.1016/j.carbon.2016.02.011.

[29] K.V. Greco, A. Forner-Cuenca, A. Mularczyk, J. Eller, F.R. Brushett, Elucidating the nuanced effects of thermal pretreatment on carbon paper electrodes for vanadium redox flow batteries, ACS Appl. Mater. Interfaces 10 (2018) 44430–44442, https://doi.org/10.1021/acsami.8b15793.

[30] F. Tariq, J. Rubio-Garcia, V. Yufit, A. Bertei, B.K. Chakrabarti, A. Kucernak, N. Brandon, Uncovering the mechanisms of electrolyte permeation in porous electrodes for redox flow batteries through real time in situ 3D imaging, Sustain. Energy Fuels 2 (2018) 2068–2080, https://doi.org/10.1039/C8SE00174J.

[31] Y.A. Gandomi, D.S. Aaron, J.R. Houser, M.C. Daugherty, J.T. Clement, A. M. Pezeshki, T.Y. Ertugrul, D.P. Moseley, M.M. Mench, Critical review—experimental diagnostics and material characterization techniques used on redox flow batteries, J. Electrochem. Soc. 165 (2018) A970–A1010, https://doi.org/10.1149/2.0601805jes.

[32] N. Ge, S. Chevalier, J. Hinebaugh, R. Yip, J. Lee, P. Antonacci, T. Kotaka, Y. Tabuchi, A. Bazylak, Calibrating the X-ray attenuation of liquid water and correcting sample movement artefacts during in operando synchrotron X-ray radiographic imaging of polymer electrolyte membrane fuel cells, J. Synchrotron Radiat. 23 (2016) 590–599, https://doi.org/10.1107/S1600577515023899.

[33] S. Chevalier, N. Ge, M.G. George, J. Lee, R. Banerjee, H. Liu, P. Shrestha, D. Muirhead, J. Hinebaugh, Y. Tabuchi, T. Kotaka, A. Bazylak, Synchrotron X-ray radiography as a highly precise and accurate method for measuring the spatial distribution of liquid water in operating polymer electrolyte membrane fuel cells, J. Electrochem. Soc. 164 (2017) F107–F114, https://doi.org/10.1149/2.0041702jes.

[34] S. Chevalier, J. Lee, N. Ge, R. Yip, P. Antonacci, Y. Tabuchi, T. Kotaka, A. Bazylak, Operando measurements of liquid water saturation distributions and effective diffusivities of polymer electrolyte membrane fuel cell gas diffusion layers, Electrochim. Acta 210 (2016) 792–803, https://doi.org/10.1016/j.electacta.2016.05.180.

[35] U.U. Ince, H. Markötter, N. Ge, M. Klages, J. Haußmann, M. Göbel, J. Scholta, A. Bazylak, I. Manke, 3D classification of polymer electrolyte membrane fuel cell materials from in-situ X-ray tomographic datasets, Int. J. Hydrogen Energy 45 (2020) 12161–12169, https://doi.org/10.1016/j.ijhydene.2020.02.136.

[36] M. Mortazavi, A.D. Santamaria, V. Chauhan, J.Z. Benner, M. Heidari, E.F. Médici, Effect of PEM fuel cell porous media compression on in-plane transport phenomena, J. Power Sources Adv. 1 (2020) 100001, https://doi.org/10.1016/j.powera.2020.100001.

[37] L. Wang, J. Wang, P. Zuo, Probing battery electrochemistry with in operando synchrotron X-ray imaging techniques, Small Methods 2 (2018) 1700293, https://doi.org/10.1002/smtd.201700293.

[38] S.-M. Bak, Z. Shadike, R. Lin, X. Yu, X.-Q. Yang, In situ/operando synchrotron-based X-ray techniques for lithium-ion battery research, NPG Asia Mater. 10 (2018) 563–580, https://doi.org/10.1038/s41427-018-0056-z.

[39] R. Banerjee, N. Bevilacqua, A. Mohseninia, B. Wiedemann, F. Wilhelm, J. Scholta, R. Zeis, Carbon felt electrodes for redox flow battery: impact of compression on

transport properties, J. Energy Storage 26 (2019) 100997, https://doi.org/10.1016/j.est.2019.100997.
[40] L. Xiao, M. Luo, L. Zhu, K. Duan, N. Bevilacqua, L. Eifert, R. Zeis, P. Sui, Pore-Scale characterization and simulation of porous electrode material for vanadium redox flow battery: effects of compression on transport properties, J. Electrochem. Soc. 167 (2020) 110545, https://doi.org/10.1149/1945-7111/aba4e3.
[41] D. Zhang, A. Forner-Cuenca, O.O. Taiwo, V. Yufit, F.R. Brushett, N.P. Brandon, S. Gu, Q. Cai, Understanding the role of the porous electrode microstructure in redox flow battery performance using an experimentally validated 3D pore-scale lattice Boltzmann model, J. Power Sources 447 (2020) 227249, https://doi.org/10.1016/j.jpowsour.2019.227249.
[42] P. Trogadas, O.O. Taiwo, B. Tjaden, T.P. Neville, S. Yun, J. Parrondo, V. Ramani, M.-O. Coppens, D.J.L. Brett, P.R. Shearing, X-ray micro-tomography as a diagnostic tool for the electrode degradation in vanadium redox flow batteries, Electrochem. Commun. 48 (2014) 155–159, https://doi.org/10.1016/j.elecom.2014.09.010.
[43] R. Jervis, L.D. Brown, T.P. Neville, J. Millichamp, D.P. Finegan, T.M.M. Heenan, D. J.L. Brett, P.R. Shearing, Design of a miniature flow cell for in situ x-ray imaging of redox flow batteries, J. Phys. D Appl. Phys. 49 (2016) 434002, https://doi.org/10.1088/0022-3727/49/43/434002.
[44] M. Gebhard, M. Schnucklake, A. Hilger, M. Röhe, M. Osenberg, U. Krewer, I. Manke, C. Roth, X-Ray-Computed radiography and tomography study of electrolyte invasion and distribution inside pristine and heat-treated carbon felts for redox flow batteries, Energy Technol. 8 (2020) 1901214, https://doi.org/10.1002/ente.201901214.
[45] L. Eifert, N. Bevilacqua, K. Köble, K. Fahy, L. Xiao, M. Li, K. Duan, A. Bazylak, P. Sui, R. Zeis, Synchrotron X-ray radiography and tomography of vanadium redox flow batteries—cell design, electrolyte flow geometry, and gas bubble formation, ChemSusChem 13 (2020) 3154–3165, https://doi.org/10.1002/cssc.202000541.
[46] SGL Carbon, Data Sheet: SIGRACELL® Battery Felts - Virgin and Thermal Activated Electrodes Made from Carbon and Graphite Felt, 2019.
[47] A.M. Pezeshki, J.T. Clement, G.M. Veith, T.A. Zawodzinski, M.M. Mench, High performance electrodes in vanadium redox flow batteries through oxygen-enriched thermal activation, J. Power Sources 294 (2015) 333–338, https://doi.org/10.1016/j.jpowsour.2015.05.118.
[48] B. Sun, M. Skyllas-Kazacos, Modification of graphite electrode materials for vanadium redox flow battery application—I. Thermal treatment, Electrochim. Acta 37 (1992) 1253–1260, https://doi.org/10.1016/0013-4686(92)85064-R.
[49] T.W. Wysokinski, D. Chapman, G. Adams, M. Renier, P. Suortti, W. Thomlinson, Beamlines of the biomedical imaging and Therapy facility at the Canadian light source - Part 2, J. Phys. Conf. Ser. 425 (2013), 072013, https://doi.org/10.1088/1742-6596/425/7/072013.
[50] J. Hinebaugh, P.R. Challa, A. Bazylak, Accounting for low-frequency synchrotron X-ray beam position fluctuations for dynamic visualizations, J. Synchrotron Radiat. 19 (2012) 994–1000, https://doi.org/10.1107/S0909049512039118.
[51] Q. Xu, T.S. Zhao, C. Zhang, Performance of a vanadium redox flow battery with and without flow fields, Electrochim. Acta 142 (2014) 61–67, https://doi.org/10.1016/j.electacta.2014.07.059.
[52] Z. Sun, J.C. Santamarina, Haines jumps: pore scale mechanisms, Phys. Rev. E. 100 (2019), 023115, https://doi.org/10.1103/PhysRevE.100.023115.